CFD analysis of the hydrodynamic performance of two candidate America's Cup AC33 hulls

Trans RINA, Vol 154, Part B1, Intl J Small Craft Tech, 2012 B1-B12

CFD ANALYSIS OF THE HYDRODYNAMIC PERFORMANCE OF TWO CANDIDATE AMERICA'S CUP AC33 HULLS

I M Viola, formerly Yacht Research Unit, The University of Auckland, New Zealand;
Since September 2010, School of Marine Science and Technology, Newcastle University, UK
R G J Flay, Yacht Research Unit, The University of Auckland, New Zealand
R Ponzini, High-Performance Computing Group, CILEA Consortium, Italy
(DOI No: 10.3940/rina.ijsct.2012.b1.113)

SUMMARY

The Computational Fluid Dynamics analysis of the hydrodynamic performance of two America's Cup design candidates is presented. Two fully appended hulls were tested in a *free to sink and trim* condition at Froude numbers ranging from 0.22 to 0.44. The experimental data of the first of the two hulls was known *a priori* and was used to investigate several computational parameters (topology and resolution of the grid, time step, discretization order, initial and boundary conditions). This hull was also used to perform the verification and validation of the numerical model at a Froude number of 0.22. The resistance was computed within an uncertainty of 2.2% at the 95% confidence level, while the numerical/experimental error was lower than 0.8%. The validated model was used to compute the resistance of the two hulls at the other Froude numbers. The maximum numerical/experimental error across all the tested Froude numbers was 1.3% and 4.1% for the two hulls respectively. Different ways of computing the skin friction are discussed and an approach to reduce the effect of numerical ventilation using the source term in the *vof* transport equation is recommended. Finally, the scalability of the code for parallel processing was tested and it was found that 32 processes enabled a 20 times speed up compared to a serial computation

1. INTRODUCTION

1.1 STATE OF THE ART

In the last 10 years, Computational Fluid Dynamics (CFD) has become more and more important in the design process of high performance yachts. In 1995, when the 29th America's Cup was sailed in San Diego between Sail America (Dennis Conner) and Team New Zealand (Peter Blake), most of the research was performed with experimental tests, both in towing tanks and in wind tunnels. New experimental facilities dedicated to sailing yachts grew up. For instance, the Yacht Research Unit Twisted Flow Wind Tunnel at the University of Auckland (Flay, 1996) was built in 1994 to support Team New Zealand, which won the cup. Numerical codes were used both for aerodynamic and hydrodynamic investigations, but these codes were not able to model viscous effects. Numerical codes, which solve the viscous Navier-Stokes equations, (called CFD codes in the present paper) were initially used to compute the aerodynamics of spinnakers in 1993 (Hedges, 1993). In the 30th America's Cup, which was sailed in 2000 in Auckland between Team New Zealand and Luna Rossa, inviscid codes became important design tools, both for designing upwind sails (Fallow, 1996) and for computing the hydrodynamic resistance of hulls (Caponnetto *et al.* 1998). It was estimated (Caponnetto, 2009) that 1/3rd of the research was conducted with inviscid numerical codes, whilst 2/3rd of the research was conducted with experimental techniques. In the 31st America's Cup, which was sailed in 2003 in Auckland between Team New Zealand and Alinghi, for the first time hydrodynamic research was performed mainly with numerical codes instead of experimental techniques. In fact CFD codes were mainly used both for aerodynamics of downwind sails (for instance, see the development of the Virtual Wind Tunnel, Richter *et al.* 2004) and for hull hydrodynamics (Azcueta 2002). The following America's Cup sailed in Valencia in 2007 between Alinghi and Team New Zealand confirmed the growing trend of increased use of numerical codes. Finally, in the last America's Cup, which was sailed in 2010 in Valencia between BMW Oracle Racing and Alinghi with extremely large multi-hulls under the Dead of Gift, CFD was the fundamental design tool, where experimental techniques were mainly used to validate numerical codes. Figure 1 shows the relative usage in percentage of numerical and experimental methods in the last five America's Cups.

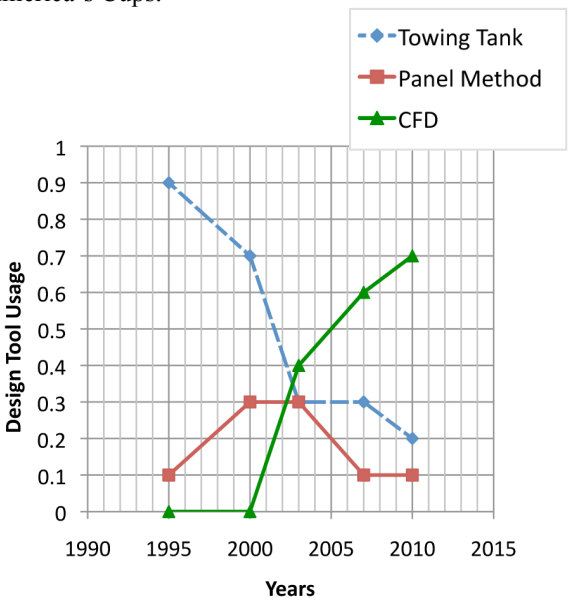

Figure 1: Design tool use in the past 5 America's Cups (data edited from Caponnetto, 2009).

1.2 THE NEED FOR VALIDATION

It must be noted that the impressive growing trend of the use of the numerical codes does not mean that experimental techniques will be completely substituted by CFD analysis in the future. In fact, validation of numerical codes is a fundamental aspect of CFD at relatively high Reynolds numbers, *Re. For s*ailing yacht hydrodynamics, *Re* is of the order of (O(-)) $Re=O(10^8)$, whilst for sail aerodynamics $Re=O(10^6)$. In order to directly solve the Navier-Stokes equations (DNS approach), the number of degrees of freedom required is of $O(\mathrm{Re}^{11/4})$ are necessary. Yacht hydrodynamics and sail aerodynamics would require the number of degrees of freedom to be of $O(10^{22})$ and $O(10^{16})$, respectively. At the current state of the art, such a large number of degrees of freedom cannot be solved by any computer and therefore, turbulence has to be modelled with simplified heuristic approaches, which must be validated with experimental measurements.

The growth of computational capabilities will increase the use of CFD codes further. Commercial codes are becoming easier to use and allow more complex physics to be modelled. Ten years ago, the differences between numerical and experimental resistances measured on a bare hull were of O(10%) (Azcueta, 2001), whilst the present publication shows differences on fully appended hulls of O(1%). The increase in accuracy allows CFD analysis to be used as a reliable design tool. Experimental tests are a more consolidated approach and the reliability of the results has been proven by experience. On the contrary, CFD is a younger science and the results need to be carefully validated. Unfortunately, in yacht design applications, only global parameters are available for validation, typically the resistance, and the sink and trim from a towing tank test performed in *free to sink and trim* conditions. Measurements of the flow patterns around the hull, pressure and skin friction distributions on the hull surface are rarely available.

1.3 ACCURACY AND COMPUTATIONAL EFFORT

CFD use as a tool in yacht design practice must be achievable with reasonable computational resources, and requires a compromise between the computational effort and the accuracy of the result. The accuracy in the computation of hull resistance required by yacht designers is of O(1%), which is also the order of magnitude of the repeatability of the towing tank (Brown *et al*, 2002). Hence, a verification and validation procedure should be performed very carefully in order to assess the uncertainty of the computed results. In particular, a comparison between the resistance measured experimentally and computed by one simulation is not sufficient to prove the accuracy of the model, because a specific set of chosen parameters might lead to the sum of large positive and large negative errors, giving a small overall error. A good simulation should achieve a small overall error, resulting from the sum of small errors. A verification and validation procedure should show that the overall error is sufficiently small to allow the resistance to be predicted with the required level of accuracy.

In the present paper, one simulation setup, described in Section 2, was verified and validated at one Froude number. Details of the verification and validation procedure are provided in Section 3. Several parameters such as grid resolution, time step, discretization order, etc. were investigated and are discussed in Section 4. Then, the validated setup was used to compute the resistance sink and trim of both the hulls at a range of Froude numbers, and the results are presented in Section 5.

2. METHOD

An America's Cup (AC) team provided the Yacht Research Unit (YRU) with two hull geometries, both candidates for the 34th America's Cup. Figure 2 shows the main dimensions of the two geometries, identified as TH04 and TH06 respectively. Note that TH04 has rounded sections, whilst TH06 has "U" shaped sections and a larger block coefficient. The AC team provided the YRU with the towing tank data for TH04 but, until the end of the project, did not provide the towing tank data for TH06.

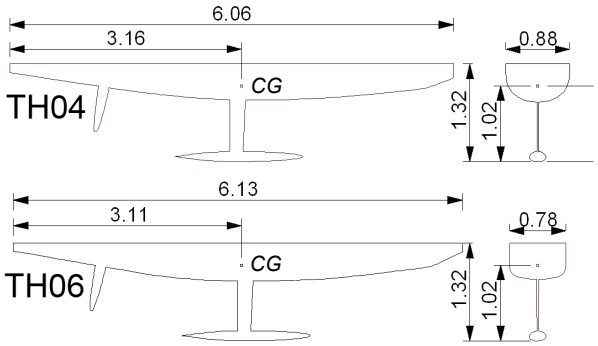

Figure 2: Main dimensions (in metres) for the two hull geometries studied.

2.1 EXPERIMENTAL METHOD

The towing tank tests were performed on 1/4th scale models in *free to sink and trim* conditions in calm water. The model-scale centres of gravity, *CG*, were located on the *flotation waterplane in measurement condition,* (*MWL*). The procedure to measure *MWL* is defined by the America's Cup Class Rule Version 5.0 (2003). The measurement condition was different from the sailing condition and, hence, *MWL* was different from the static water-plane of the tested condition.

The *CG* was in different position in full scale and model scale. Thus for each tested condition, a different pitching

moment was applied to the model in order to take into account the effect of the full-scale *CG* position and of the aerodynamic forces.

Boat speeds *(BS)* from 6 to 12 knots full-scale were tested, which convert to 3 to 6 knots in model-scale, and correspond to Froude numbers *(Fr)* from 0.22 to 0.44.

The models were tested in *free to sink and trim* conditions and the resistance, sink and trim were measured for each *BS*. The models were fully appended, and zero leeway and heel angles were used.

2.2 NUMERICAL METHOD

The commercial code STAR-CCM+ (CD-adapco) version 4.06.011 was used. The model-scale towing tank experiments were modelled.

The incompressible Navier-Stokes equations were solved with an implicit unsteady solver. Both the air and water densities were assumed to be constant and hence, the energy equation was not solved. Numerical schemes with second-order in space and first-order in time accuracy, respectively, were used to solve the discrete system. The convective equation was solved with a blending function between an upwind scheme and a centred scheme.

The κ–ε *realizable* turbulent model was used. Several grids were tested but none of them solved the boundary layer over the entire hull and the appendages. Therefore, the boundary layer was modelled with wall functions. The *two-layer all* y^+ *wall treatment* was used (see User Guide STAR-CCM+ Version 4.06.011 for details). The *all* y^+ formulation switches from the traditional wall-function approach to the traditional low-Reynolds number approach, using a blending function, *g*, which is a function of the Reynolds number based on wall distance. The *two-layer* formulation for the κ–ε *realizable* turbulent model, switches to a one-equation model in the near-wall region, which solves κ but prescribes ε algebraically as a function of the wall distance (Rodi, 1991).

2.2.1 VOLUME OF FLUID

A *volume of fluid* (VOF) technique was used to model the two-phases, air and water. This approach assumes that the two phases in a control volume share the same velocity, pressure and temperature. The continuity and momentum equations are solved for a mixed fluid, whose density ρ and viscosity μ are calculated on the basis of the volume of fluid of each phase. The volume of fluid, *vof,* is defined as the ratio between the volume occupied by the phase and the volume of the control volume. In particular:

$$\rho = vof_{air} \cdot \rho_{air} + vof_{water} \cdot \rho_{water} \tag{1}$$

$$\mu = vof_{air} \cdot \mu_{air} + vof_{water} \cdot \mu_{water} \tag{2}$$

$$vof_{air} = 1 - vof_{water} = \frac{V_{air}}{V_{water} + V_{air}} \tag{3}$$

The volume of fluid is computed with an additional transport equation:

$$\frac{\partial}{\partial t}\int_V vof + \oint_{\partial V} vof \cdot (\boldsymbol{u} - \boldsymbol{u}_G) = \int_V S \tag{4}$$

Where ∂V is the surface of the control volume V, $\mathbf{u}$ is the velocity vector of the mixed fluid, $\mathbf{u}_G$ is the velocity vector of the grid and S is a *vof* source term, which is usually set to zero.

2.2.1 TWO DEGREES OF FREEDOM

The hull motion can be taken into account using one of two approaches. The first approach, named *morphing*, moves the hull in the computational domain and re-computes the grid at each time step. This approach is computationally demanding due to the re-meshing procedure. The second approach, which was used in the present work, moves the entire domain with respect to the free surface. Therefore, the mesh does not change, and the boundary conditions are updated at each time step.

The *six degrees of freedom* (*DOF*) module with updating boundary conditions was used to model sink and trim. The forces acting on the hull are computed at each iteration and the following equations of motion are solved to compute the vertical velocity w and the pitch angular velocity ω_y of the hull:

$$M \cdot \frac{dw}{dt} = F_z \tag{5}$$

$$I_y \cdot \frac{d\omega_y}{dt} = M_y \tag{6}$$

Where M is the hull mass, F_z the vertical force acting on the *CG*, I_y the second principal moment of inertia, and M_y the moment acting on the model around the y-axis.

2.2.3 BOUNDARY CONDITIONS

The lengths of the model-scale waterlines were roughly L=5 m for the two hulls. L was assumed to be a reference length to build the computational domain. A right rectangular prism 2L high, 2L wide and 5L long was used. The origin was located at the intersection between the forward perpendicular, MWL and the symmetry plane of the hull. The distance from the origin of the axis system to the front, top, bottom and sides of the prism faces was L, whilst the downstream face was 4L from the origin. A pressure outlet boundary condition was used on the latter face, whilst an inflow boundary condition was used on the other prism faces. For each *BS*, the inflow condition was a constant uniform velocity profile. At the

inlet, vof_{air}=0 and vof_{water}=1 were set below the waterline, and vof_{air}=1 and vof_{water}=0 were set above the waterline. The turbulence intensity was set to 0.01 and the turbulent viscosity ratio was set to 10. At the outlet, the net pressure *p,* defined as the difference between the static pressure and the hydrostatic pressure, was set to p=0 Pa.

2.2.4 HARDWARE

The grids were developed on a desktop workstation, located at the YRU in Auckland (New Zealand), equipped with Intel Core 2 Quad Q9300 processors, 4 GB of 800 MHz RAM, and using Linux Suse OS. The simulations were run on the CILEA cluster in Milan (Italy) and were remotely managed by the YRU using the PBS-Professional (Altair Inc.) workload system. The cluster, named *Lagrange*, is made up of 208 2-way nodes Intel Xeon 3.16 GHz QuadCore with 16 GB per node, running Red Hat Enterprise Linux Server (Release 5.1) OS. The number of cores used ranged from 8 to 128 depending on the grid dimensions. More than 200 runs were performed and more than 200,000 hours of total wall time, defined as the product of the wall time of each simulation and the number of cores, were computed.

3 VERIFICATION

A rigorous verification and validation (V&V) procedure, as suggested by Stern et al (2006), was performed and is summarised herewith.

3.1 V&V DESCRIPTION

The difference between a computed value S and a true value T is the simulation error E. This is due to the numerical error δ_{SN} - which includes errors due to the iteration number δ_i, grid size δ_g, time step δ_t, and other input parameters δ_p - and to the numerical modelling δ_{SM}, as defined in Eq (7)

$$E = S - T = \delta_{SN} + \delta_{SM} = (\delta_i + \delta_g + \delta_t + \delta_p) + \delta_{SM} \quad (7)$$

The verification process assesses the numerical uncertainty U_{SN} at the 95% confidence level due to the numerical error δ_{SN}. In particular, it assesses the uncertainty components due to the iteration number U_i, grid size U_g, time step U_t, and other input parameters U_p.

The validation process assesses the modelling uncertainty U_{SM} due to the modelling error δ_{SM}. The overall simulation uncertainty is estimated as per experimental fluid dynamics uncertainty analysis, shown in Eq (8).

$$U_S^2 = U_{SN}^2 + U_{SM}^2 = (U_i^2 + U_g^2 + U_t^2 + U_p^2) + U_{SM}^2 \quad (8)$$

The uncertainties due to the grid size U_g and time step U_t are evaluated by performing several simulations with different grid sizes and time steps. Increasing the spatial and time resolutions should cause the solution to converge (monotonically or oscillating) to a grid-size and time-step independent solution. Grids that are too coarse, and time steps that are too large lead to non-converging trends and unreliable solutions. If a convergent trend is achieved, U_g and U_t are estimated on the basis of the order of convergence. Convergence analysis (*Richardson Extrapolation, RE*) also allows the numerical solution S to be extrapolated to infinitely high spatial and time resolutions.

Validation is performed by comparing the numerical solution S with the experimental results D. The uncertainty of the validation U_{val} is due to the numerical uncertainty U_{SN} and to the experimental uncertainty U_D, calculated according to Eq. (9).

$$U_{val}^2 = U_{SN}^2 + U_D^2 \quad (9)$$

A simulation is validated if the absolute value of the error $E = |S - D|$ is smaller than the validation uncertainty U_{val}. In fact, the validation uncertainty is a measure of the 'noise' in the comparison between the numerical and experimental data. If the error is lower than the noise then the simulation is validated and no conclusions can be drawn about the modelling error. Conversely, if the error is larger than the noise then the simulation is not validated and the error is (partially) due to modelling error.

3.2 VERIFICATION OF THE NUMERICAL INVESTIGATION

The verification procedure was performed at *Fr*=0.22 by performing both a spatial and a time resolution investigation. Four similar grids were developed with ICEM-CFD by increasing the node distance by a factor $\sqrt[3]{2}$. Therefore the node distances of the finest grid, with about 4 million cells, were half the node distances of the coarsest grid, with about 500,000 cells. Note that only a half domain was modelled, to take advantage of the symmetry plane of the yacht. The results shown in Section 5 were achieved with the second coarsest grid, named the *base grid*. This grid was also used to perform a time resolution investigation. Simulations were performed with 5 inner iterations and time steps of 0.02, 0.01, 0.005 and 0.0025 s. The time step used in Section 5 is 0.005 s, namely the *base time step*.

The coarsest grid and the largest time step did not lead to convergent trends. Conversely, the 3 finest grids and the 3 smallest time steps led to high-order converging trends. Figure 3 shows the total resistance computed with these 3 grids and 3 time steps, divided by the resistance computed using the base grid and base time step. The 3 simulations with different spatial resolutions have relative step sizes of $1/\sqrt[3]{2} = 0.79$, 1, and $\sqrt[3]{2} = 1.26$;

while the 3 simulations with different time resolutions have relative step sizes of 0.5, 1 and 2.

The orders of convergence for the spatial and time resolutions were used to compute the extrapolated values *(RE)* for infinitively fine grids and infinitively small time steps, in order to determine the grid (U_g) and time (U_t) uncertainties. The extrapolated resistances in space and time are 1.7% and 0.5% lower than the base resistance respectively (Figure 3). The grid and time uncertainties computed using the extrapolated values are both smaller than 0.1%, while the grid and time uncertainties computed at the base grid and time step are $U_g = 2.1\%$ and $U_t = 0.6\%$ respectively.

The uncertainties due to the iteration number U_i and to the other parameters U_p are estimated to be much smaller than U_g and U_t. Therefore the numerical uncertainty of the base simulation is computed using Eq. (10).

$$U_{SN} = \sqrt{U_g^2 + U_t^2} = 2.2\% \qquad (10)$$

In Figure 3, the error bar shows the numerical uncertainty of the base simulation.

The nominal accuracy of the resistance measurement is ±1% (Brown et al. 2002). It is common practice to measure the resistance several times at each *BS* and then to fit the data with a cubic spline. The scatter from such measurements is of order ±2% (Brown et al. 2002). Figure 3 shows also the experimental resistance (divided by the base simulation resistance) and the error bar shows its uncertainty.

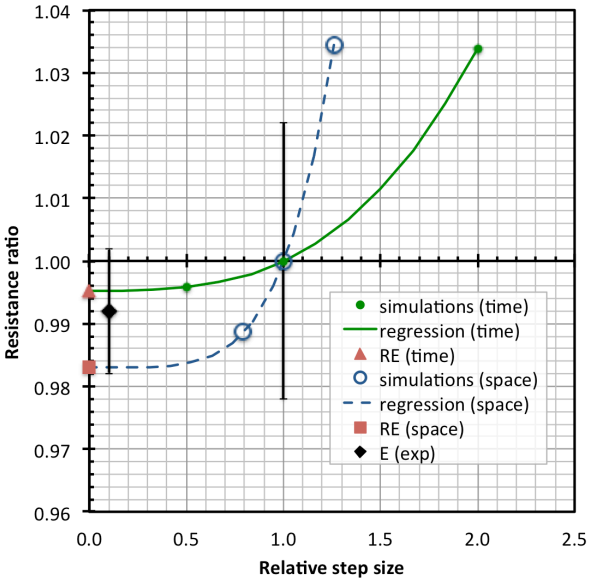

Figure 3: Resistance ratio for 3 different grid sizes and 3 different time steps.

The validation uncertainty, computed with Equation (9), is $U_{val} = 2.4\%$, which is larger than the simulation error $E = -0.8\%$, computed with Equation (7). Therefore the numerical simulation has been successfully validated.

4. RESULTS AND DISCUSSION

In this section the insight gained from the findings resulting from the main parameters investigated are presented and discussed.

4.1 GRIDS

Two grid types were tested. Hexahedral non-structured non-conformal grids were made with STAR-CCM+ (CD-adapco), and block-structured conformal grids were made with ICEM-CFD (Ansys). It should be noted that STAR-CCM+ is a face-based non-structured solver. Hence, the terms non-conformal and structured are referred to the grids and not to the way that the solver manages the grids.

In the non-structured non-conformal grids performed with STAR-CCM+, the domain is filled with hexahedra, which are trimmed by the hull. Each hexahedron can be halved along any of its sides. For instance, figure 4A, shows the bow of TH04 modelled with this approach, where the two colours show the two phases. Figure 4B shows the contours of net pressure near the keel/bulb region of TH04. The grid is made up of large hexahedra (top left of figure 4A and 4B), which are horizontally and/or vertically halved. The boundary layer is modelled with prismatic cells. The method is very interesting because it allows automatic grid generation, which is an important feature to use to compare different geometries. This approach allows the grid resolution to be increased in the wave pattern region only around the hull if desired.

In the block-structured conformal grids, performed with ICEM-CFD, the domain is divided into blocks. Figure 5A shows the bow of TH06 modelled with this approach, where the two colours show the two phases. Figure 5B shows the contours of net pressure in the keel/bulb region of TH06. This approach allows a rectangular surface grid to be achieved, where the edges are aligned and stretched along the main flow direction, which improves the computation of the fluid in the boundary layer.

The two approaches were investigated with several different grids for TH04, with various numbers of cells and various criteria for grid refinement. It was found that modelling the boundary layer with low grid resolution causes the friction resistance to be over-estimated. Conversely, modelling the wave pattern with low grid resolution lead to a smoother wave pattern and, hence, the pressure resistance was under-estimated. However, this latter effect is generally less significant than the former. Therefore, the overall resistance decreases when the node distances of the entire domain are decreased.

The wall-distance, $y+$, of the first cell centre was investigated in the range $y+\approx30$ and $y+\approx300$. It was

found that the friction resistance decreased asymptotically when y+ decreased. Hence, $y+\approx30$ is recommended from this work. Lower $y+$ values require very fine grids or highly stretched hexahedra, and cause *numerical ventilation,* which is discussed below, to increase. For these reasons, the base grids described in Sections 3 and 5 have $y+\approx30$.

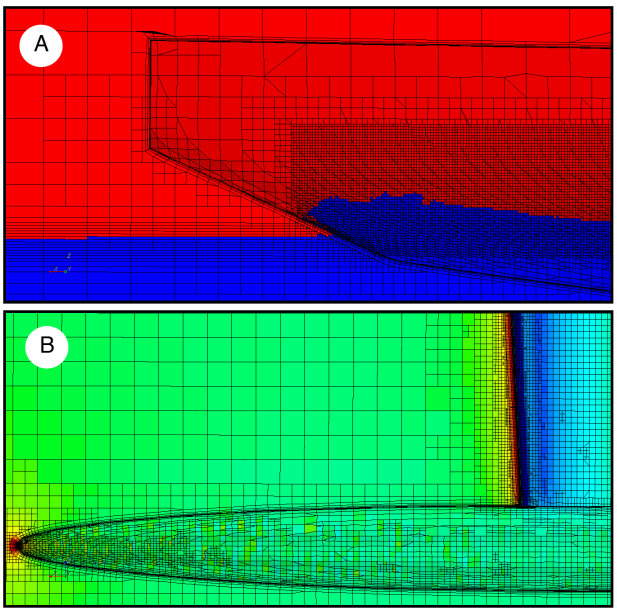

Figure 4: Bow (A) and keel/bulb region (B) of TH04 modelled with a hexahedral non-structured non-conformal grid.

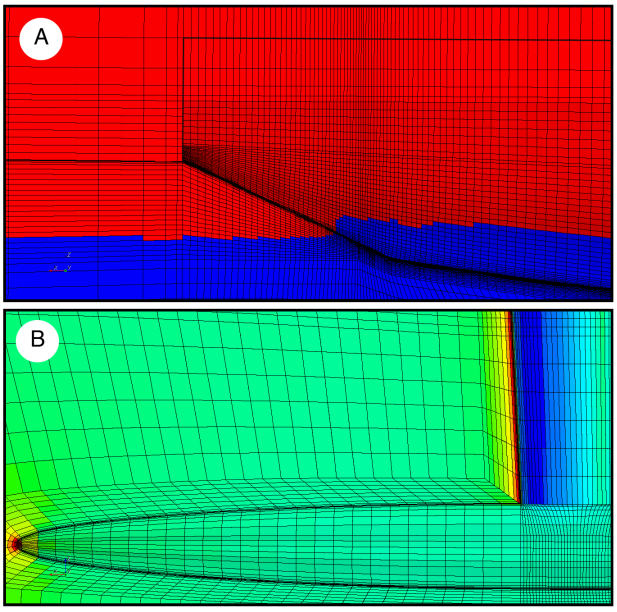

Figure 5: Bow (A) and keel/bulb region (B) of TH06 modelled with a block-structured conformal grid.

The wave pattern should be modelled with high grid resolution in the region around the hull to correctly model the near-wall waves. Conversely, the wave pattern over the rest of the domain should be intentionally modelled with low grid resolution to increase the amount of numerical diffusion, which damps the flow pattern and reduces wave reflections at the boundaries. For instance, figure 6 shows the wave pattern around TH04 at *BS*=12 knots full-scale (*Fr*=0.44). The grid in the figure allows wave reflection to be avoided, as shown by the contours of the vertical height of the free surface. In the latest version of STAR-CCM+ (V5.04), the wave reflection at the boundaries can also be damped by adding a resistance term to the equation for the vertical flow velocity component.

The grids for the TH04 model made with both STAR-CCM+ and ICEM-CFD gave very similar results. On the basis of the present research, it is not possible to recommend one or other of the two approaches as being superior.

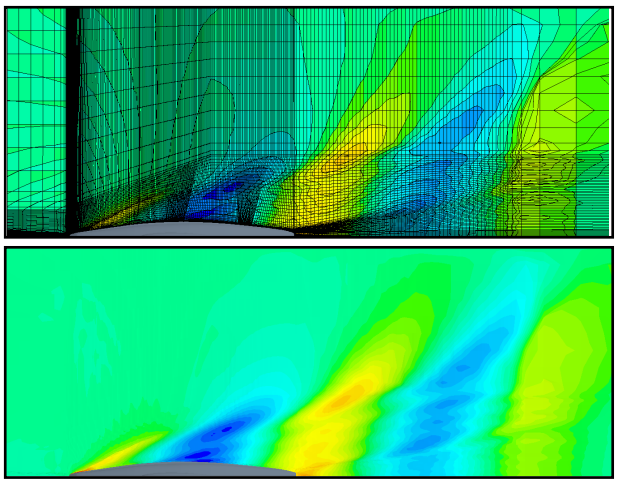

Figure 6: The grid (upper) and wave pattern (lower) for TH04 at *BS*=12 knots full-scale (*Fr*=0.44).

4.2 DISCRETISATION ORDER

First order accuracy was used for the transient terms (Euler Implicit) as it was found that using second order accuracy led to instabilities on the water surface. Conversely, second order discretisation was found to be the most appropriate for the convection terms of the fluid, turbulence and VOF equations. Modelling the convection terms using first order has three undesirable consequences. Firstly, the computed resistance increases due to the increase in numerical diffusion. Secondly, the *numerical ventilation increases*, as described below. Finally, the thickness of the region enlarges where the cells have a mixture of the two phases. In fact, when second order is used, the transition between the air and the water occurs in a couple of cells, whereas when first order is used, this transition occurs through a much larger number of cells, due to the numerical diffusion of vof_{water} and vof_{air}.

A test simulation was performed with different discretisation orders for the convection terms of the VOF, turbulence and fluid equations respectively. The

resistances computed using first order for only one of the VOF, turbulence and fluid equations, were 6%, 27% and 30% respectively, larger than when using the second order for all the equations. The resistance computed using first order for the convection term for all the equations was 41% larger than when using second order.

4.3 2 DOF

There are several methods to start a simulation in *free to sink and trim* conditions. One method is to start the simulation with BS=0 m/s and with a constant acceleration of the hull. For instance, other authors (e.g. Azcueta 2002) have used a constant acceleration of 0.1 m/s^2. Another method consists of performing a preliminary simulation where none of the DOF are released. In the present paper, it was found that solving for less than 10s was long enough to achieve a converged simulation. Then the DOF are successively released using a ramp function. If necessary, additional damping terms, proportional to the sink and trim velocities, can be added to the sink and trim equations to improve the convergence. The STAR-CCM+ user manual recommends this method. A third method consists of starting the simulation with the DOF released and without a ramp function. This method could lead to divergence or to fast convergence depending on how far the initial values of sink and trim are from the final values. If good approximations of sink and trim are provided as the initial conditions, a converged solution can be achieved after solving for 30 s. However, because sink and trim vary with the BS, for each BS different initial values should be used. In the present paper, this was achieved by using different initial grid positions for each BS.

In the present investigation, the movement of the hull was modelled by rigidly moving the grid with respect to the free surface. It was found that the boundary condition variation at each time step lead to fluctuations of the water plane height, which were transported through the domain, and this can affect the convergence of the simulation. It was found that in the first few seconds of the simulation the hull moved from its initial position to the equilibrium position. However, its inertia caused it to go past the equilibrium position. Therefore, the boat reached the equilibrium position by following a damped oscillatory movement. These oscillations of the hull caused the inlet boundary condition to oscillate, as shown in figure 7, which shows a schematic drawing of the first 2 seconds of one of the simulations performed. At t=0.0 s the boat is set at a raised position compared to the final state. At t=0.3 s, the stern has sunk more than the bow, leading to a negative (bow-up) trim. Thus, the water plane is re-set to $z=-z_1$ at the boundary inlet. At t=1.2 s the boat has sunk to the final position but the bow has sunk more than the stern. Hence, the boat has sunk correctly, but has a positive trim. Thus, the water plane at the boundary inlet was set to $z=z_2$. Finally, at t=2.0 s the bow has risen up to its final position. Hence, the boat has sunk and has negative trim. During the 1.7 s period between 0.3 s and 2.0 s, the height of the water plane at the boundary inlet oscillated with an amplitude of $\Delta z=z_2-z_1$. As a consequence, a wave with the period of $T\approx$1.7 s and a wavelength of $\lambda=BS\cdot T\approx$5 m (using BS=3 m/s), has been generated and is moving along the computational domain. In this example, after 2.0 s the hull had reached its equilibrium position, but had to face a wave with a wavelength equal to its waterline length.

The initial oscillations of the sink and trim of the hull caused the height of the water plane at the boundary inlet to oscillate. Such oscillations introduce a wave into the computational domain, which can induce a further oscillation of the sink and trim of the hull. This wave can affect the convergence significantly. To minimise the wave amplitude due to trim oscillations, the upstream inlet face should be as close as possible to the boat. In the present paper, one boat length was used. If the final sink and trim are known, these values should be used as the initial conditions. When the trim is modelled, the pitching inertia can be used to speed up the convergence. In the present paper, the weight of the experimentally tested boat that was roughly 400 *kg* and this value was used in the numerical model, while the moment of inertia I_y was unknown. Several values of I_y between I_y =8 kg·m to I_y =8,000 kg·m were tried in the simulations, and it was found that I_y =80 kg·m gave the optimum convergence.

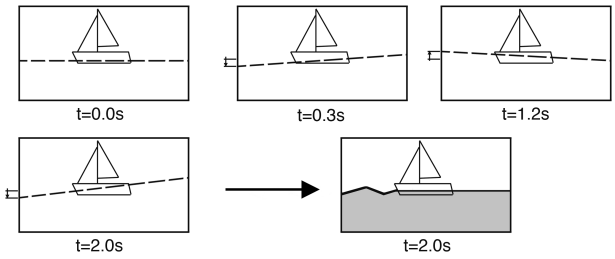

Figure 7: Schematic drawing of the free surface perturbation due to the moving grid.

4.4 SKIN FRICTION

The computation of skin friction is often affected by *numerical ventilation*, which occurs when particles of air are trapped into the boundary layer and transported below the water plane. This problem is well known in the field by CFD users and vendors. However, it has rarely been mentioned or discussed in scientific publications. The amount of air in the boundary layer depends on the grid resolution, the hull geometry, and on the BS. Air is located in only the first few cells near the wall. Therefore, the air is confined to a very small fraction of the boundary layer thickness. However, the shear stress is incorrectly computed by using the properties of this mixed fluid, instead of using the properties of water.

The wall function computes the friction velocity u^* using equation (11).

$$u^* = \sqrt{g \cdot \frac{\nu u}{y} + (1-g) \cdot C_\mu^{1/2} \cdot k} \qquad (11)$$

where

$g = \exp\left(-\frac{1}{11} \cdot \mathrm{Re}_y\right)$ is the *all-y*$^+$ blending function, $\mathrm{Re}_y = \sqrt{k}\frac{y}{\nu}$ is a wall-distance-based Reynolds number, ν is the kinematic viscosity, u is the tangential velocity, y is the wall distance, C_μ=0.09 is a constant, and k is the turbulent kinetic energy.

Equation (11) shows that u^* is over-estimated when numerical ventilation occurs. This is because ν for the mixed fluid is higher than ν for water. However, the effect of ν is smoothed by the blending function g and becomes negligible for low-resolution grids (because Re_y is large and $g \approx 0$). The wall function also computes a production term for k and algebraically prescribes the value of the turbulent dissipation rate ε, which are both functions of u^*. When low-resolution grids are adopted, these terms are not affected significantly by the numerical ventilation, because the over-estimation of u^* is negligible. In the present paper, and in most of the engineering applications in this field, the grid resolution in the near-wall region is low (typically $y^+ > 30$), and hence the over-estimation of u^* is negligible.

The shear *stress* τ_w *is* computed from u^* using equation (12).

$$\tau_w = \rho \cdot \left(u^*\right)^2 \qquad (12)$$

Equation (12) shows that if the error in the computation of u^* is negligible, then the shear stress is under-estimated due to numerical ventilation. This is because the error in estimating the shear stress is proportional to the vof_{air}., as shown in Eq. (13) formed by combining Eqs. (1) and (12).

$$\tau_w = (vof_{air} \cdot \rho_{air} + vof_{water} \cdot \rho_{water}) \cdot (u^*)^2$$
$$= \tau_{water} - vof_{air} \cdot (\rho_{water} - \rho_{air}) \cdot (u^*)^2 \qquad (13)$$

Equation (13) suggests that the shear stress τ_w computed by the solver could be corrected to that of pure water by adding the last term of the equation onto the computed value of τ_w.

In the present paper, the skin friction resistance σ was computed by integrating u^* over the wetted surface A_w and then multiplying it by the water density as shown in Equation (14).

$$\sigma = \rho_{water} \cdot \int_{A_w} \left(u^*\right)^2 \qquad (14)$$

This method does not take into account the over-estimation of u^* due to the wall function. Hence, it would not be suitable if the grid in the boundary layer were highly refined.

A_w should be defined appropriately, by considering the shape of the bow waves. It is common practice to define the free surface with an iso-surface where vof_{water}=vof_{air}=0.5. However, due to numerical diffusion, which tends to increase the amount of air in the mixed fluid, a lower value of vof_{water} can be considered. A lower value of vof_{water} significantly affects the region of the bow wave where the transition between vof_{water}=0 and vof_{water}=1 occurs over several cells, while it is negligible downstream and in the rest of the wave pattern. In the present paper, values between 0.2 and 0.5 were used to investigate the iso-surface for different grids. In the results presented in Section 5, the same value was used across all the tested BS.

Numerical ventilation can be avoided by using a negative source term S (i.e. a sink) in Equation (4) for the air phase. In particular, where the vof_{water} is greater than 0.5 and the wall distance is lower than an arbitrary distance d, S can be defined as a fraction $1/n$ of $-vof_{air}$. Therefore, in n iterations, the source S would extract all the air in the cell. Similarly, it is also possible to add a source term for the water phase in order to confine the transition from water to air across only one cell. In particular, where the vof_{air} is greater than 0.5 and the wall distance is lower than an arbitrary distance d, S can be defined as a fraction $1/n$ of $-vof_{water}$. Therefore, in n iterations, the source S would extract all the water in the cell.

For instance, Figure 8 shows the contours of vof_{air} on the bow of TH04 at $Fr = 0.44$ computed without (Figure 8A) and with (Figure 8B) phase sources for the air and the water. While Figure 8B shows a clear transition from $vof_{air} = 0$ in blue below the free surface, and $vof_{air} = 1$ in red above the free surface, Figure 8A shows a wide region along the hull where $0 < vof_{air} < 1$.

In this example, $d = 0.002\ mm$ and $n = 300$. Using 3 inner iterations and a time step of 0.01 s, the source S extracts all the undesired air and water within 1 s.

This method was tested in the present paper but not used to achieve the results presented in Section 5. However, preliminary results show that it is an efficient way of avoiding numerical ventilation, and it should be explored further. A preliminary verification analysis showed that this method leads to very similar grid and time uncertainties to the method presented in Equation (14). Moreover, the coarsest grid and the largest time step used in Section 3 led to converging trends when sources were used, and led to diverging trends when the Eq. (14) method was used. It should be noted that where one phase is extracted and the other phase is injected, the continuity equation is violated. However, this resulted to

be negligible, as also shown by the small effect on the residuals.

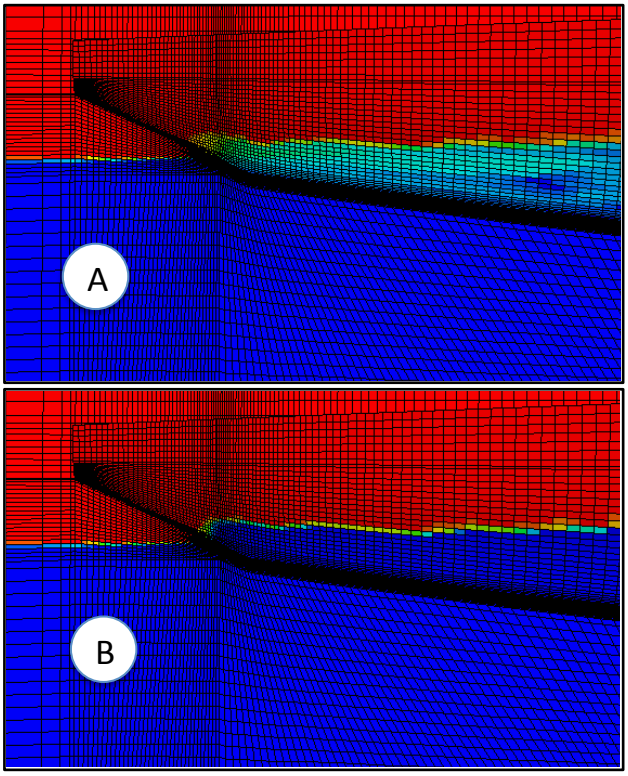

Figure 8: TH04 at *Fr* = 0.44 modelled without (A) and with (B) sources for the volumes of fluid.

4.5 TIME STEP SIZE

Time steps from *ts*=0.02 s to *ts*=0.0025 s were tested. The grid size in the stream-wise direction is roughly 0.03 m and 0.01 m on the hull and on the keel respectively. Hence the Courant numbers, *Co,* based on the *BS* were between *Co=0.1* and *Co*=6. Increasing the time step causes the numerical ventilation to increase and thus the friction resistance to decrease. In particular, 4 simulations were performed where the time step was successively doubled each time, and the friction resistance always decreased. The simulation with the largest time step showed a friction resistance 8% lower than the simulation with the smallest time step. However, when it was re-computed to take the numerical ventilation into account as shown above, it increased by roughly 3.5% (Figure 3).

4.6 SCALABILITY

To investigate the efficiency and the scalability of the code in this application, 500 time steps were computed with a range of number of cores from 1 to 128. A half-hull was modelled with 1 million cells with STAR-CCM+. A time step *ts*=0.005 s was used with 5 inner iterations per time step. The simulation was performed at *Fr*=0.38 in a *free to sink and trim* condition. After 7,500 time steps, the simulation was stopped and 500 time steps were performed on a serial processor, and on parallel processors with 2, 4, 8, 16, 32, 64, 128 cores respectively. The parallel processes were performed in batch mode with MPI drivers and an Infiniband connection. The total wall time, defined as the product of the wall time of each simulation and the number of cores, increased significantly for 64 and 128 cores. Figure 9 shows the efficiency, defined as the ratio of the wall time of the serial process to the total wall time of the parallel process. The efficiency decreased to roughly 0.7 with 32 cores and then dropped further with 64 and 128 cores. The speed up shown in Figure 10, which is defined as the ratio between the wall time of the serial process to the wall time of the parallel process, shows that 32 cores allow the simulation to be run roughly 20 times faster than a serial process, but that increasing the number of cores further does not result in an increased speed up.

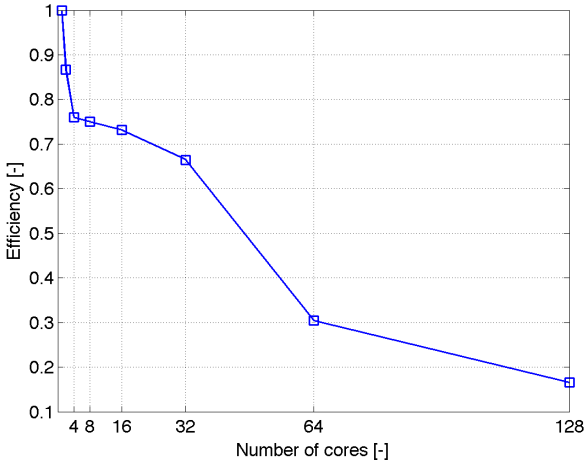

Figure 9: Efficiency of the computations versus number of cores.

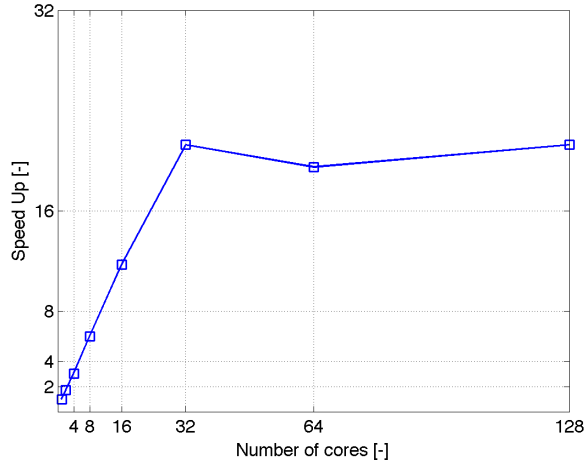

Figure 10: Speed up versus number of cores.

It was noted *a posteriori* that at each time step the distance of each cell from the nearest wall was recomputed. This computation could have been avoided. CD-adapco suggested that avoiding this computation leads to a better scalability.

Additional tests were performed with grids developed with ICEM-CFD and very similar results were achieved.

In the present paper, most of the simulations were performed with 32 cores. A few simulations with grids of more than 2 million elements were also performed with 64 cores.

5. NUMERICAL/EXPERIMENTAL COMPARISON

5.1 TH04 COMPARISON

The same settings used in Section 3 were used to compare the numerical/experimental resistance, sink and trim at different *Fr*. In particular, the base grid and base time step with 5 inner iterations were used

The computed resistance, sink and trim showed good agreement with the experimental data. Figure 11 shows the numerical and the experimental resistance of TH04 at various *Fr*. The maximum differences in the resistance of TH04 is 1.3% at $Fr = 0.38$. It should be reiterated that the uncertainty in the experimental data was estimated to be about 1% and that the verification procedure (Section 3) performed at $Fr = 0.22$ showed a numerical uncertainty of 2.2%.

Figure 12 shows the numerical and the experimental trim of TH04 at various *Fr* with reference to the static trim. While the relative trim differences between various speeds of TH04 show a numerical/experimental agreement of ±0.01 deg, the CFD systematically under-predicts the trim by about 0.02 deg. This shift is very small and is probably smaller than the experimental uncertainty. In fact, over the length of the static water line, 0.02 deg of trim results in forward and aft draft changes that are smaller than 0.9 mm.

Figure 13 shows the numerical and experimental sink of TH04 at various *Fr* with reference to the static sink. CFD under-predicts the sink from 1.4 mm to about 3.8 mm when *Fr* increases from 0.22 to 0.44. Further investigations are needed to clarify the reasons for this mismatching.

5.2 TH04 VERSUS TH06

TH06 was modelled with the same numerical conditions (grid resolution, time step, discretisation order, etc.) as TH04.

The a posteriori comparison of the computed resistance of TH06 with the experimental data showed good agreement. In particular, the maximum difference was 4.1% at $Fr = 0.29$. While the relative resistance differences for the various speeds showed a numerical/experimental agreement of ±0.9%, CFD systematically under-estimated the resistance by about 2.5%.

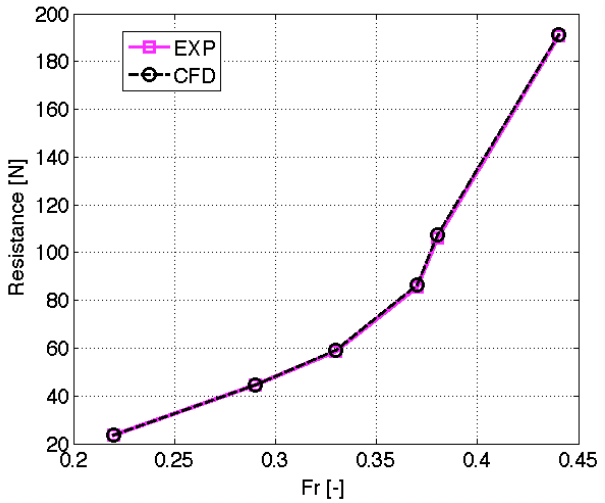

Figure 11: Numerical and experimental resistances for TH04.

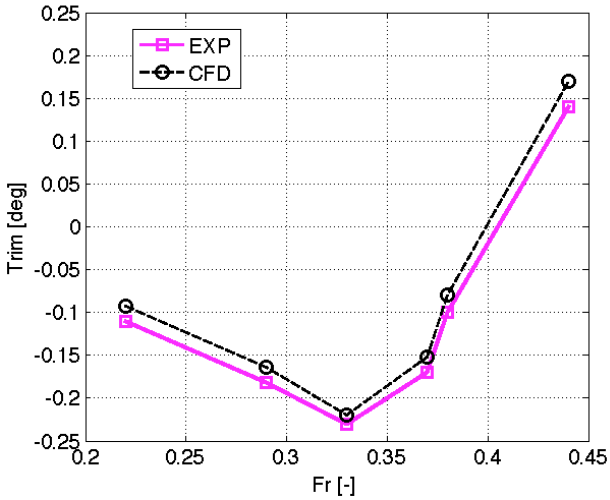

Figure 12: Numerical and experimental trims for TH04.

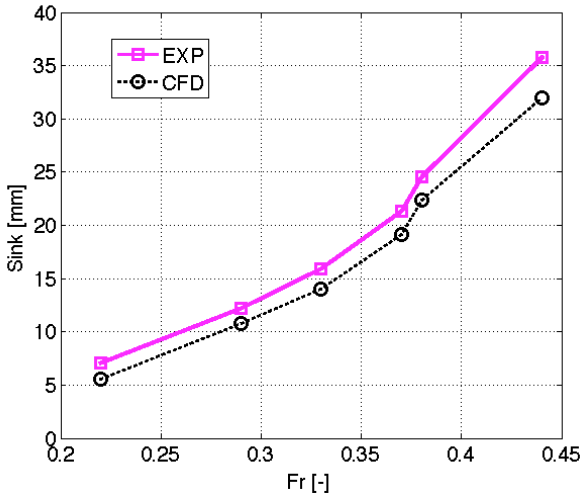

Figure 13: Numerical and experimental sinks for TH04.

Despite the differences between the two geometries, the two hulls show very similar resistances. TH04 performs better at low *Fr*, while TH06 performs better at high *Fr*. The cross-over is at around 10 knots full-scale (*Fr*=0.37). Both hulls are in the displacement mode in the range of the *Fr* investigated. Increasing *Fr* causes the pressure resistance to increase more than the friction resistance, and hence the higher the *Fr* the larger the proportion of pressure resistance compared to friction resistance (Figure 14). The two hulls have very similar friction resistances. Conversely, TH04 has a larger pressure resistance at low *Fr* and a lower pressure resistance at high *Fr* compared to TH06.

Figure 15 shows the resistance difference between the two geometries at various full-scale boat speeds. CFD predicted the performance cross-over at 9.5 knots, while the towing tank showed the cross-over at 10.3 knots. Hence, the numerical and the experimental results would have led to the same choice between the two geometries at all boat speeds, except in a range between 9.5 and 10.3 knots.

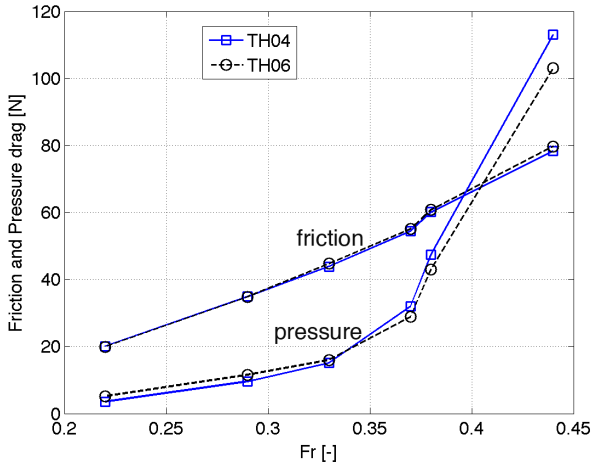

Figure 14: Computed friction and pressure resistance of the TH04 and TH06.

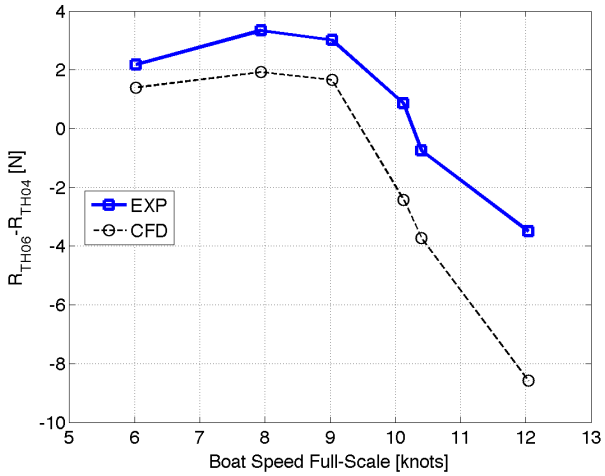

Figure 15: Resistance differences between the TH06 and TH04 models.

6. CONCLUSIONS

In the present paper the hydrodynamic performance of two America's Cup hulls were computed with CFD and compared with towing tank data. The uncommon characteristics of this comparison are that it was performed:

1. With fully appended hulls
2. In *free to sink and trim* conditions
3. Not knowing *a priori* the experimental data for the second of the two hulls (TH06)

The numerical/experimental differences of the resistance are of the order of 1%. In particular, the computed resistance was in very good agreement with the experimental data for the first (TH04) of the two hulls, while it was under-estimated by about 2.5% for the second hull (TH06).

The maximum numerical/experimental differences were 1.3% and 4.1% for the two hulls respectively.

If the experiment or the computations were used to choose the boat with the lower resistance, the same choice would have been made for most of the boat speeds. In a small boat speed range, around 10 knots full scale, the experiment and the CFD would have led to different choices.

Several simulations of the first hull (TH04) were performed, comparing numerical results with experimental data, which were known *a priori*. This allowed the effect of several computational parameters to be investigated and their effect to be discussed.

GRIDS

Hexahedral non-structured non-conformal grids and block structured conformal grids were tested. The former allow the wave pattern to be modelled with high resolution, while the latter allow a regular surface grid to be achieved on the hull surface. The two grid types perform similarly and not one of them could be recommended above the other. Grids with about 2,000,000 cells for a domain containing only a half–hull, and with $y+$ about 30 allowed the accuracy required in yacht design practice to be achieved.

DISCRETISATION ORDER

The use of first order accuracy is suggested for the transient terms, whilst second order accuracy is suggested for the convection terms. Using second order accuracy in time led to instabilities, whilst using first order accuracy in space led to resistance over-estimation.

2 DOF

Sink and trim were modelled with a rigid motion of the whole domain with respect to the free surface. This technique lead to instabilities in the free surface when an impulsive start was adopted, which affected the

convergence. It was found that changing the pitching inertia and the distance from the bow to the upstream boundary face could be used to decrease the oscillation of the solution.

SKIN FRICTION

It was found that skin friction is affected by *numerical ventilation*. It is recommended that the alternative method to compute the skin friction, which takes into account the *numerical ventilation,* is used. Using a source term in the phase transport equation was found to allow *numerical ventilation* to be avoided. However, additional tests are necessary before this practice can be recommended.

TIME STEP

Time steps from *ts*=0.02 s to *ts*=0.0025 s were tested. Decreasing the time step caused the *numerical ventilation* to decrease, which caused the friction resistance to increase. However, if the friction resistance is computed with the proposed method described in the paper, which takes into account the *numerical ventilation*, the friction resistance decreases due to lower numerical diffusion.

SCALABILITY

To investigate the scalability of the code in this application, 500 time steps of the same simulation with 1 million cells were computed by different number of cores from 1 to 128. The results showed that the efficiency decreases to roughly 0.7 with 32 cores, and then decreased further to roughly 0.3 with 64 cores.

7. ACKNOWLEDGMENTS

The support of CD-adapco is gratefully acknowledged. In particular, the authors are grateful to Demetris Clerides and Anthony Massobrio for supporting the project, to Carlo Pettinelli for his suggestions, and to Paul Bosauder (Matrix Applied Computing Ltd) for high-quality technical support.

8. REFERENCES

America's Cup Class Rule Version 5.0, Challenger of Record and Defender for America's Cup XXXII, 15th December 2003, 32nd.americascup.com/en/acclopaedia/ /texts/acc_rules.php

AZCUETA R, Computational of Turbulent Free Surface Flows Around Ships and Floating Bodies, *PhD Thesis, Technical University Hamburg-Harburg, Germany*, 2001.

AZCUETA R, RANSE Simulations for Sailing Yachts Including Dynamic Sinkage & Trim and Unsteady Motions in Waves, *in the proceedings of The 1st High Performance Yacht design Conference, Auckland,* 4th-6th December 2002.

BROWN M, CAMPBELL I, ROBINSON J, The Accuracy and Repeatability of Tank Testing, from Experience of ACC Yacht Development, in the proceedings of *The 1st High Performance Yacht Design Conference, Auckland, New Zealand,* 4th-6th December 2002.

CAPONNETTO M, Solutions for Marine Applications, *CD-adapco Marine Webinar*, 22nd January 2009, www.cd-adapco.com/applications/marine.html

CAPONNETTO M, CASTELLI A, BONJOUR B, MATHEY PL, SANCHI S, SAWLEY ML, America's Cup Yacht Design using Advanced Numerical Flow Simulations, *EPFL Super Computing Review, pp. 24-28,* November 1998.

CD-adapco, User Guide STAR-CCM+ Version 4.06.011, 2009.

FALLOW J.B., America's Cup Sail Design. *Journal of Wind Engineering and Industrial Aerodynamics*, 63, 183-192, 1996

FLAY, R.G.J., A twisted flow wind tunnel for testing yacht sails, Journal of Wind Engineering and Industrial Aerodynamics, 63, 171-182, 1996

HEDGES KL, Computer Modelling of Downwind Sails, *ME Thesis, University of Auckland, New Zealand,* 1993.

IMAS L, BAKER B, WARD B, BULEY G, CFD-Based Hydrodynamic Analysis of High Performance Racing Yachts, *in the proceedings of The 19th Chesapeake Sailing Yacht Symposium, Annapolis, Maryland, pp. 31-36,* 20th-21st March 2009.

RICHTER HJ, HORRIGAN KC, BRAUN JB, Computational Fluid Dynamics for Downwind Sails, *in the proceedings of The 16th Chesapeake Sailing Yacht Symposium,* 21st-23rd March 2003.

RODI W, Experience with Two-Layer Models Combining the k-e Model with a One-Equation Model Near the Wall, *in the proceedings of The 29th Aerospace Sciences Meeting, Reno, NV, AIAA 91-0216,* 7th-10th January 1991.

STERN, F., WILSON, R., SHAO, J., Quantitative V&V of CFD Simulations and Certification of CFD codes, *Intl. J. Numerical Methods In Fluids, vol 50, no 11, pp 1335-1355,* 20 April 2006